Supporting Information for "Barchan-barchan repulsion investigated at the grain scale"

N. C. Lima[1], W. R. Assis[1,3], C. A. Alvarez[2], E. M. Franklin[1]

[1]Faculdade de Engenharia Mecânica, Universidade Estadual de Campinas (UNICAMP),

Rua Mendeleyev, 200, Campinas, SP, Brazil

[2]Department of Earth & Planetary Sciences, Stanford University,

Stanford, CA 94305, USA

[3]Current address: Saint Anthony Falls Laboratory, University of Minnesota, Minneapolis, Minnesota, USA

Contents of this file

1. Figures S1 to S10

2. Tables S1 and S2

Additional Supporting Information (Files uploaded separately)

1. Captions for Movies S1 and S2

Introduction

This supporting information presents additional descriptions, graphics, tables, and movies showing examples of barchan-barchan interactions. All movies have been sped up by 4x. We note that numerical scripts used in the manuscript are available on Mendeley Data (http://dx.doi.org/10.17632/ypkgwjfr4r.1).

This subsection presents supplementary information concerning the materials and methods described in the paper. An even more detailed description can be found in Lima, Assis, Alvarez, and Franklin (2022).

Numerical Model

For the solid-solid contact forces and torques, $\vec{F}_c$ and $\vec{T}_c$, respectively (Equations 1 to 3 of the paper), we compute particle-particle and particle-wall contacts,

$$\vec{F}_c = \sum_{i \neq j}^{N_c} \left(\vec{F}_{c,ij} \right) + \sum_{i}^{N_w} \left(\vec{F}_{c,iw} \right) \tag{1}$$

$$\vec{T}_c = \sum_{i \neq j}^{N_c} \vec{T}_{c,ij} + \sum_{i}^{N_w} \vec{T}_{c,iw} \tag{2}$$

where $\vec{F}_{c,ij}$ and $\vec{F}_{c,iw}$ are the contact forces between particles i and j and between particle i and the wall, respectively, $\vec{T}_{c,ij}$ is the torque due to the tangential component of the contact force between particles i and j, and $\vec{T}_{c,iw}$ is the torque due to the tangential component of the contact force between particle i and the wall. N_c - 1 is the number of particles in contact with particle i, and N_w is the number of particles in contact with the wall. In Equations 1 and 2, we apply the Hertzian model, where $\vec{F}_{c,ij}$ and $\vec{F}_{c,iw}$ are decomposed into normal (Equation 3) and tangential (Equation 4) components,

$$F_{c,n} = \kappa_n \delta_n - \gamma_n \frac{d\delta_n}{dt} \,, \tag{3}$$

$$F_{c,t} = \kappa_t \delta_t - \gamma_t \frac{d\delta_t}{dt} \,, \tag{4}$$

where δ_n is the normal displacement of two objects in contact, δ_t is the tangential displacement in the direction perpendicular to the plane of contact, and κ_n, γ_n, κ_t and γ_t are coefficients linked to the properties of the considered materials. In Equation 4, $F_{c,t}$ is limited by the Coulomb's Law: once the limit of static friction is reached, $F_{c,t}$ is computed by Eq. 5 until the contact ends,

$$F_{c,t} = \mu F_{c,n} \,, \tag{5}$$

where μ is the microscopic coefficient of sliding friction.

For the fluid, we employed the so-called unresolved approach, where the equations of motion are phase-averaged (volume basis) while assuring mass conservation. In the present case, the flow was incompressible, and we used the mass (Equation 6) and momentum (Equation 7) equations of *Set II* described in Zhou, Kuang, Chu, and Yu (2010),

$$\frac{\partial \left(\alpha_f \rho_f\right)}{\partial t} + \nabla \cdot \left(\alpha_f \rho_f \vec{u}_f\right) = 0 \tag{6}$$

$$\frac{\partial \left(\alpha_f \rho_f \vec{u}_f\right)}{\partial t} + \nabla \cdot \left(\alpha_f \rho_f \vec{u}_f \vec{u}_f\right) = -\alpha_f \nabla P - \vec{f}_{exch} + \alpha_f \nabla \cdot \vec{\bar{\tau}}_f + \alpha_f \rho_f \vec{g} \tag{7}$$

where α_f is the volume fraction of the fluid, $\vec{u}_f$ is the fluid velocity, ρ_f is the fluid density, and $\vec{f}_{exch}$ corresponds to the phase-averaged forces per unit of volume that the fluid applies on solid particles,

$$\vec{f}_{exch} = \frac{1}{\Delta V} \sum_{i}^{n_p} \left(\vec{F}_d + \vec{F}_{vm}\right) \,, \tag{8}$$

where $\vec{F}_d$ is the drag force, $\vec{F}_{vm}$ is the virtual mass force, and n_p is the number of particles in a cell of volume ΔV. In our computations, we neglect Basset, Saffman and Magnus forces beacuse they are usually considered of lesser importance in CFD-DEM simulations (Zhou et al., 2010)

Numerical Setup

The distribution of grains used in each pile and their properties are available in Table S2, and the mesh used for the fluid is available in Table S1.

References

Lima, N. C., Assis, W. R., Alvarez, C. A., & Franklin, E. M. (2022). Grain-scale computations of barchan dunes. *Phys. Fluids*, *34*(12), 123320. Retrieved from https://doi.org/10.1063/5.0121810 doi: 10.1063/5.0121810

Zhou, Z. Y., Kuang, S. B., Chu, K. W., & Yu, A. B. (2010). Discrete particle simulation of particle–fluid flow: model formulations and their applicability. *J. Fluid Mech.*, *661*, 482–510.

Movie S1. aligned.mp4 Movie showing top views of the evolution of two barchan dunes interacting with each other in the aligned case. The video is sped up by 4x.

Movie S2. offcentered.mp4 Movie showing top views of the evolution of two barchan dunes interacting with each other in the off-centered case. The video is sped up by 4x.

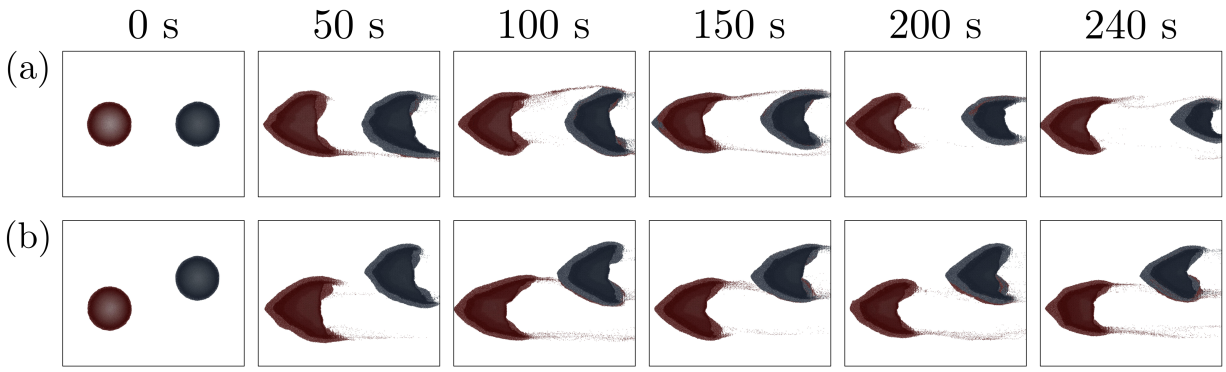

Figure S1. Snapshots showing the grains of each dune (top view) at different instants for the (a) aligned and (b) off-centered cases. Grains originally in the upstream pile are in dark-red color, while those originally in the downstream pile are dark blue.

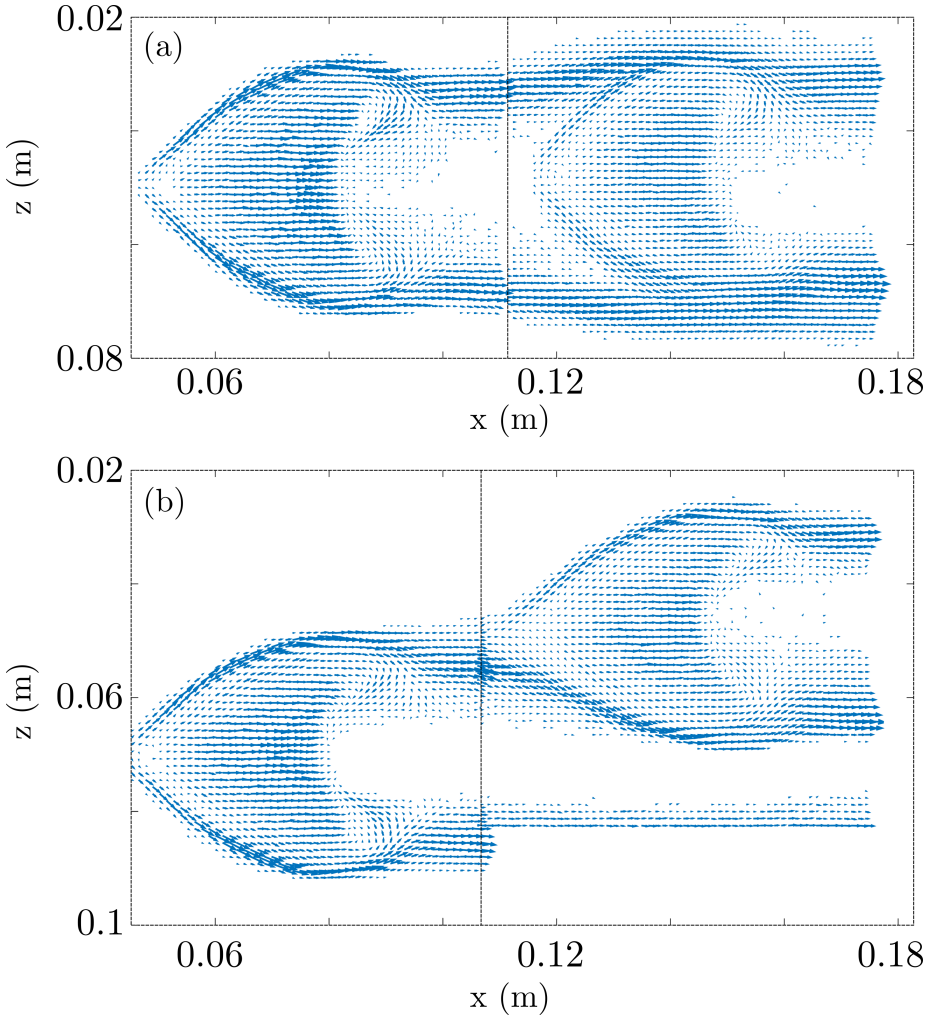

Figure S2. Time-averaged velocity fields of grains moving over barchans for the (a) aligned and (b) off-centered cases. The size of arrows is proportional to the modulus of velocity vectors.

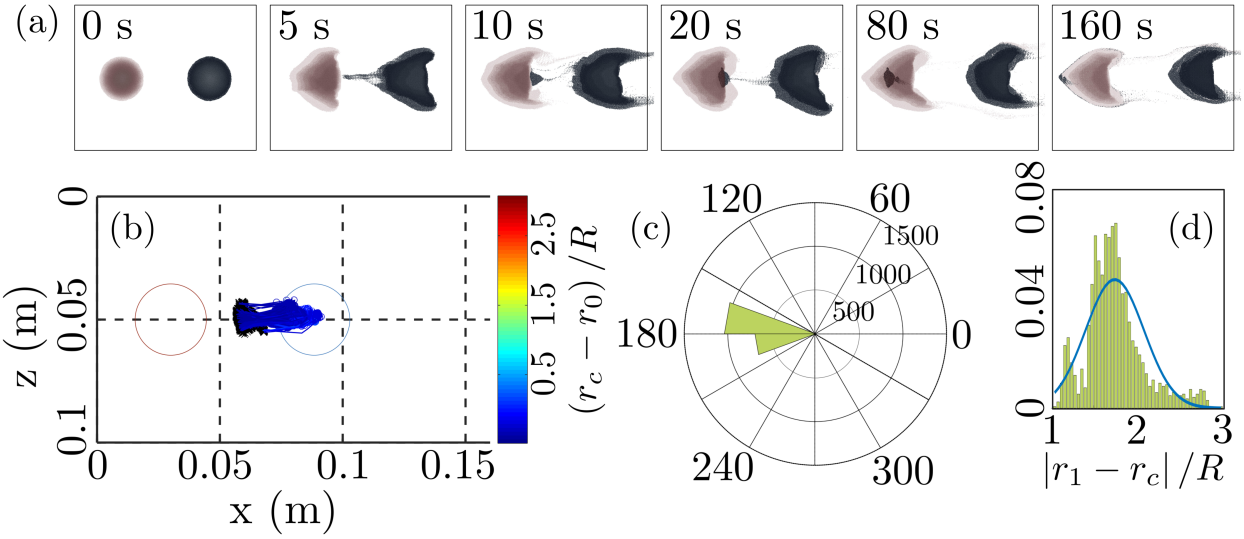

Figure S3. Mass exchange in the aligned case. (a) Snapshots with transparency showing the grains of each dune (top view) at different instants (appearing in maroon for the upstream barchan and gray for the downstream one due to the percentage of transparency adopted). (b) Trajectories of grains leaving the downstream barchan and reaching the upstream one, in which the colorbar indicates the dune longitudinal position when the considered grain started its motion. The large circles indicate the initial piles (top view), the small circles the initial position of the considered grain when it started moving on the downstream barchan, and the x's indicate their respective final positions (when stopping) on the upstream barchan. (c)–(d) Number of grains N from the downstream barchan reaching the upstream one, in polar coordinates (with origin at the centroid of the downstream barchan): (c) frequency of occurrence of N as a function of the angle (the origin is in the flow direction), and (d) pdf of N as a function of the radial position. In the figure, R is the radius of the initial pile, r_1 is the initial radial position of grains leaving the upstream barchan, and r_c and r_0 are, respectively, the instantaneous and initial positions of the centroid of the upstream dune.

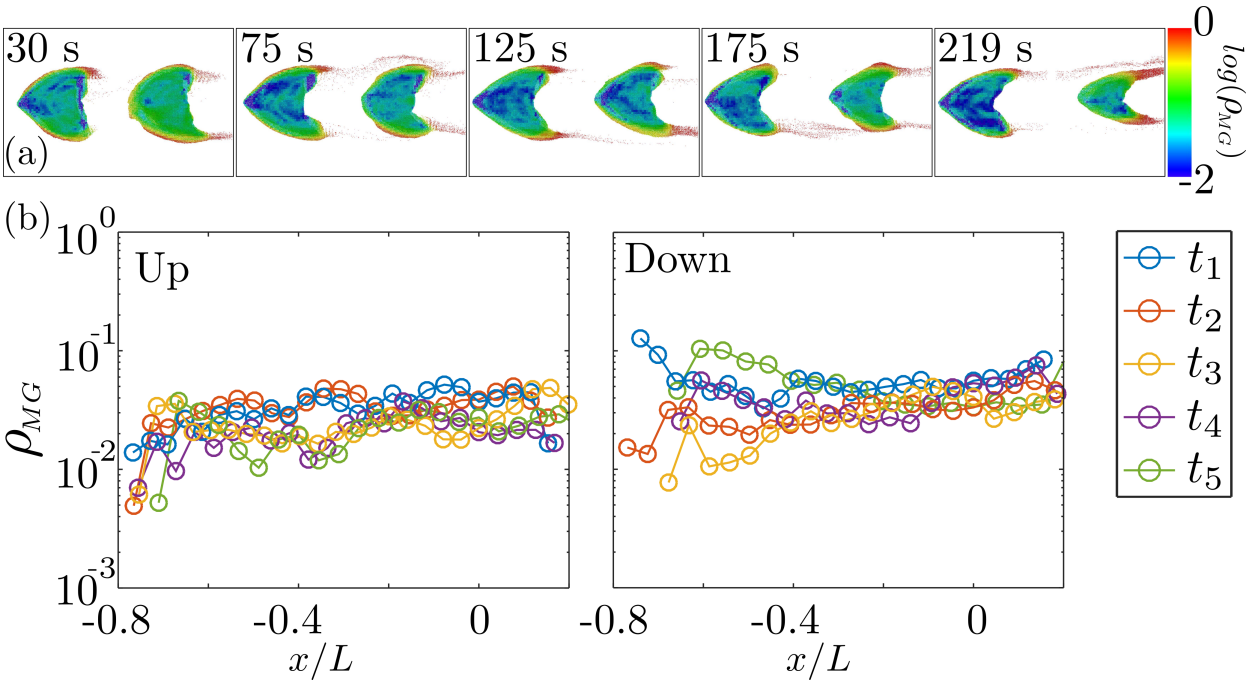

Figure S4. Density of moving grains ρ_{MG}, computed as the average number of moving grains divided by the total number of grains in each region, in the aligned case. (a) Snapshots showing the grains of each dune (top view) at different instants, colored in accordance with value of ρ_{MG} of the region they are in. The averages are computed in intervals t_1 to t_5 (t_1 = 10–50 s, t_2 = 51–100 s, t_3 = 101–150 s, t_4 = 151–200 s, t_5 = 201–238 s). (b) Density of moving grains ρ_{MG} along the barchan by considering its central slice only ($\approx$ 1.2 mm thick), averaged over the t_1 to t_5 intervals, for the upstream (Up) and downstream (Down) barchans.

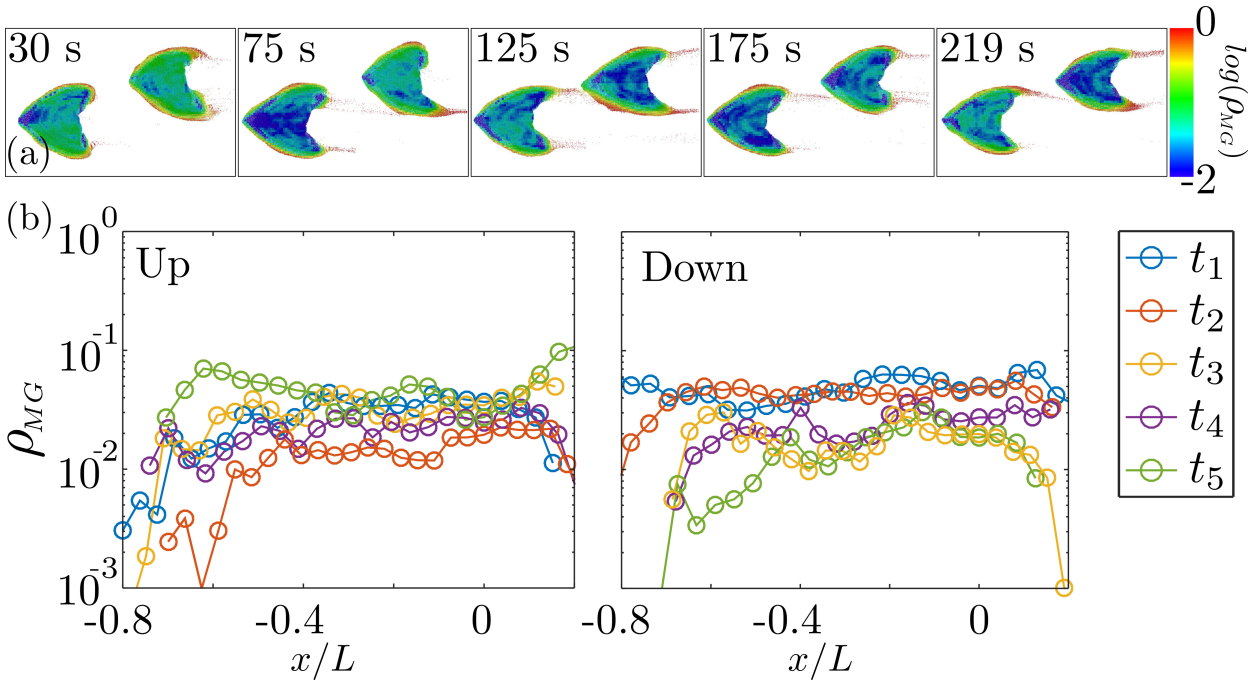

Figure S5. Density of moving grains ρ_{MG}, computed as the average number of moving grains divided by the total number of grains in each region, in the off-centered case. (a) Snapshots showing the grains of each dune (top view) at different instants, colored in accordance with value of ρ_{MG} of the region they are in. The averages are computed in intervals t_1 to t_5 (t_1 = 10–50 s, t_2 = 51–100 s, t_3 = 101–150 s, t_4 = 151–200 s, t_5 = 201–238 s). (b) Density of moving grains ρ_{MG} along the barchan by considering its central slice only ($\approx$ 1.2 mm thick), averaged over the t_1 to t_5 intervals, for the upstream (Up) and downstream (Down) barchans.

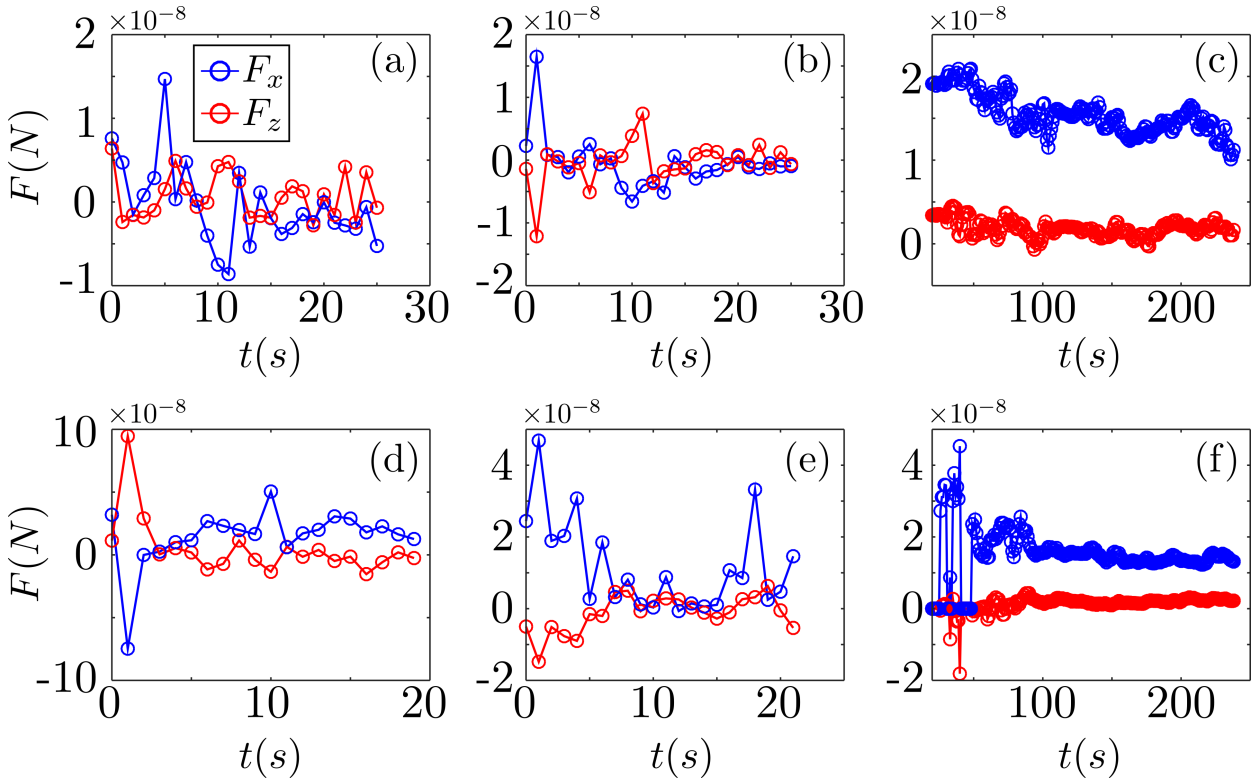

Figure S6. Longitudinal and transverse components of the resultant force on a grain, F_x and F_z, respectively, as a function of time. The instantaneous force for a specific grain (randomly chosen) migrating from the upstream dune toward the downstream one is shown for the aligned (panels a and b, each one for a specific grain) and off-centered (panels d and e, each one for a specific grain) cases. (c) and (f) Mean resultant force computed for all particles migrating from the upstream to the downstream dune (from the moment they are ejected from the upstream barchan) for the aligned (c) and off-centered (f) cases.

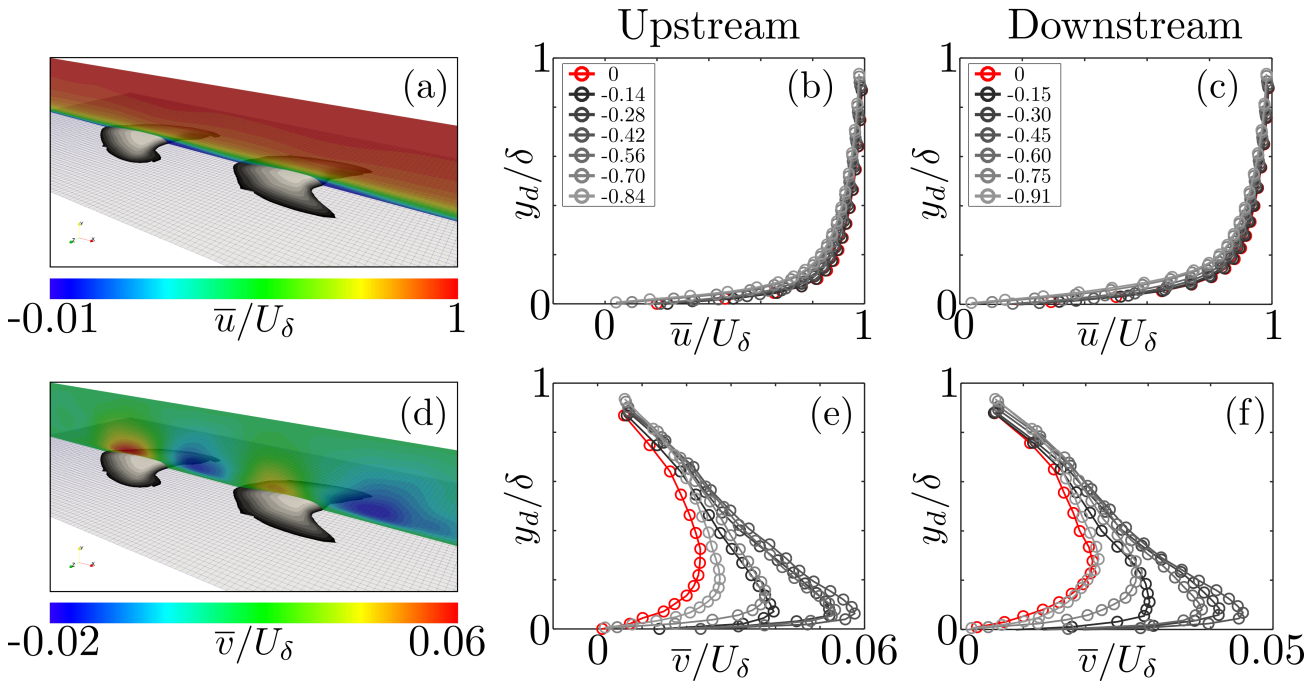

Figure S7. Water velocities in the aligned case. (a) and (d) Longitudinal and vertical components of the velocity field of the water flow, respectively, in the vertical symmetry plane. The magnitude of velocities is shown in the colorbar. (b) and (e) Vertical profiles of longitudinal $\overline{u}$ and vertical $\overline{v}$ components of the mean velocity over the upstream dune. (c) and (f) Vertical profiles of longitudinal $\overline{u}$ and vertical $\overline{v}$ components of the mean velocity over the downstream dune. The longitudinal positions of each profile, with origin at the dune crest, are shown in the figure key.

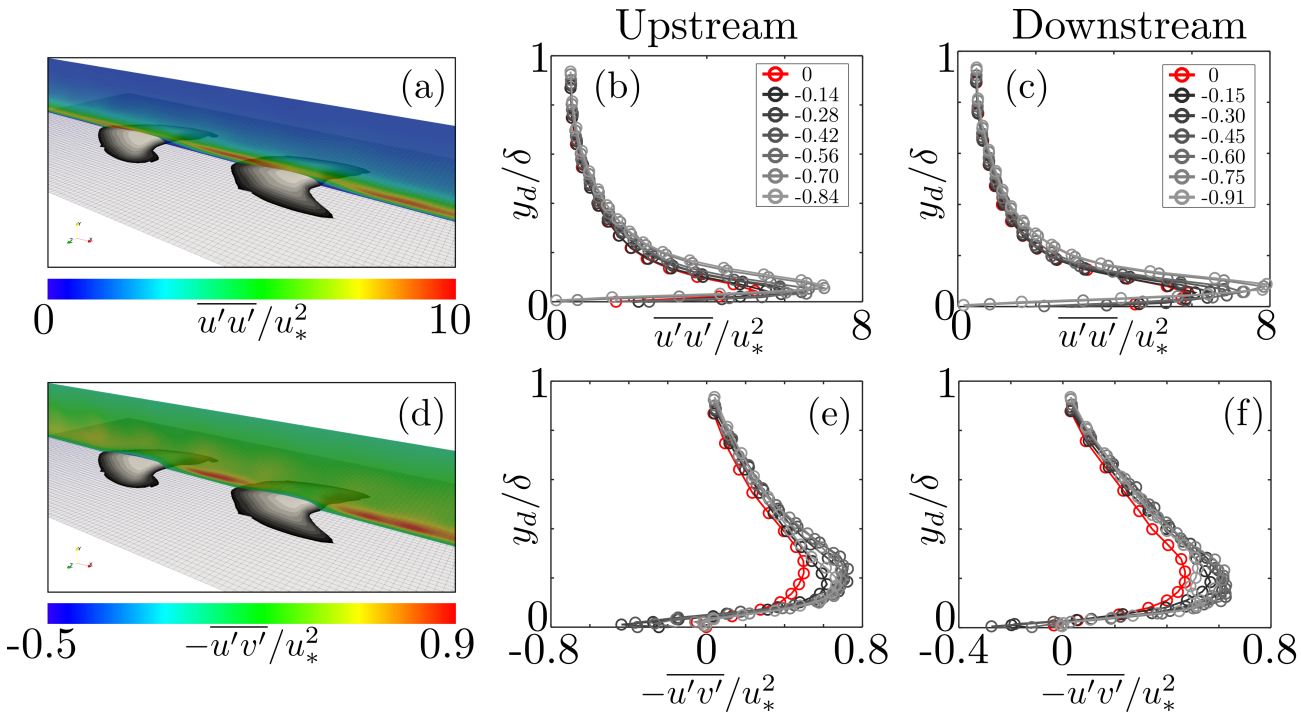

Figure S8. Second-order moments in the aligned case. (a) and (d) Longitudinal-longitudinal ($\overline{u'u'}$) and longitudinal-vertical ($-\overline{u'v'}$) components of the stress tensor, respectively, in the vertical symmetry plane. The magnitude of velocities is shown in the colorbar. (b) and (e) Vertical profiles of ($\overline{u'u'}$) and ($-\overline{u'v'}$) over the upstream dune. (c) and (f) Vertical profiles($\overline{u'u'}$) and ($-\overline{u'v'}$) over the downstream dune. The longitudinal positions of each profile, with origin at the dune crest, are shown in the figure key.

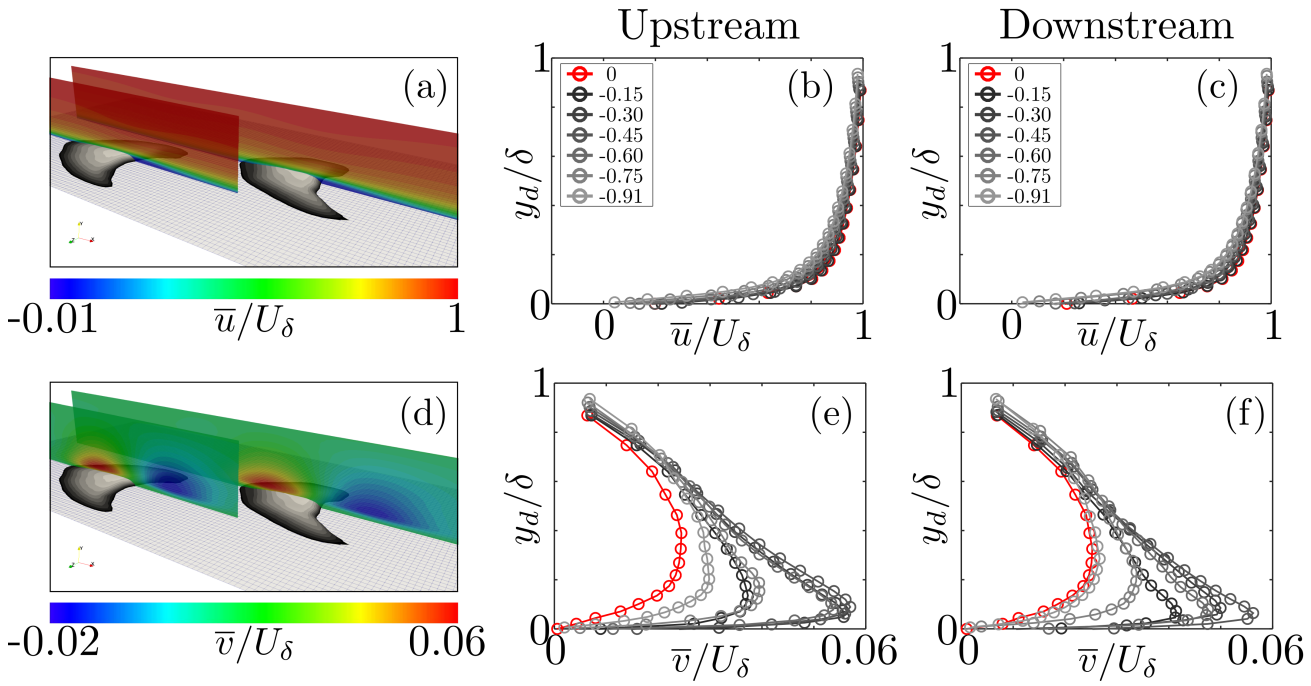

Figure S9. Water velocities in the off-centered case. (a) and (d) Longitudinal and vertical components of the velocity field of the water flow, respectively, in the vertical symmetry plane. The magnitude of velocities is shown in the colorbar. (b) and (e) Vertical profiles of longitudinal $\overline{u}$ and vertical $\overline{v}$ components of the mean velocity over the upstream dune. (c) and (f) Vertical profiles of longitudinal $\overline{u}$ and vertical $\overline{v}$ components of the mean velocity over the downstream dune. The longitudinal positions of each profile, with origin at the dune crest, are shown in the figure key.

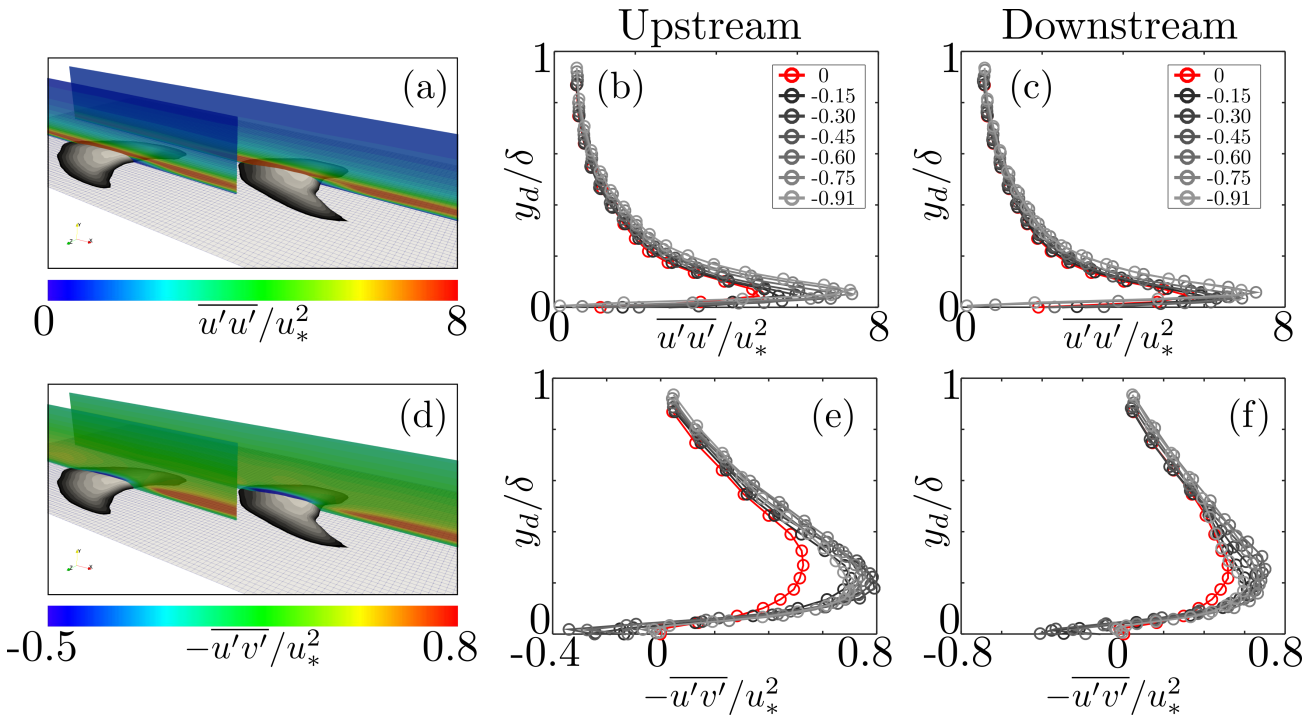

Figure S10. Second-order moments in the offcentered case. (a) and (d) Longitudinal-longitudinal ($\overline{u'u'}$) and longitudinal-vertical ($-\overline{u'v'}$) components of the stress tensor, respectively, in the vertical symmetry plane. The magnitude of velocities is shown in the colorbar. (b) and (e) Vertical profiles of ($\overline{u'u'}$) and ($-\overline{u'v'}$) over the upstream dune. (c) and (f) Vertical profiles($\overline{u'u'}$) and ($-\overline{u'v'}$) over the downstream dune. The longitudinal positions of each profile, with origin at the dune crest, are shown in the figure key.

Table S1. For the used mesh, numbers of control volumes N_{cv} and of divisions of the domain in the x, y and z directions (d_x, d_y and d_z, respectively), and vertical position of the center of the first control volume scaled in inner-wall units, y^+_{1st}.

N_{cv}	d_x	d_y	d_z	y^+_{1st}
472500	250	30	63	2.1

Table S2. Distribution of diameters for the grains in each initial pile, where N_d is the number of grains for each diameter d, and physical properties.

N_d	Diameter d (mm)	Properties	
2276	0.15	Sliding Friction Coeff. μ	0.6
13592	0.175	Rolling Friction Coeff. μ_r	0.0
68267	0.2	Restitution Coef. e	0.1
13591	0.225	Poisson Ratio σ	0.45
2274	0.25	Young's Modulus E (MPa)	5
$\cdots$	$\cdots$	Density ρ_p (kg/m^3)	2500